

Using Direct Numerical Simulation for Evaluating of Superhydrophobic Turbulent Drag Reduction

Lee Chen, Zheng Xiang , Bing Pan, Don Chen
Faculty of Computer Science and Information System
Universiti Teknologi MARA (UiTM), Malaysia

Abstract:

Superhydrophobic surfaces combine hydrophobic surface chemistry with topological microfeatures. These surfaces have been shown to provide drag reduction in laminar and turbulent flows. In this work, direct numerical simulation is used to investigate the drag reducing performance of superhydrophobic surfaces in turbulent channel flow. Slip velocities, wall shear stresses, and Reynolds stresses are determined for a variety of superhydrophobic surface microfeature geometry configurations at friction Reynolds numbers of $Re_\tau \approx 180$, $Re_\tau \approx 395$ and $Re_\tau \approx 590$. This work provides evidence that superhydrophobic surfaces are capable of reducing drag in turbulent flow situations by manipulating the laminar sublayer. For the largest micro-feature spacing, an average slip velocity over 80% of the bulk velocity is obtained, and the wall shear stress reduction is found to be greater than 50%. The simulation results suggest that the mean velocity profile near the superhydrophobic wall continues to scale with the wall shear stress and the log layer is still present, but both are offset by a slip velocity that is primarily dependent on the microfeature spacing.

I. BACKGROUND

Superhydrophobic surfaces are characterized by both chemical hydrophobicity and microscale topological roughness. The most overt physical characteristic of these surfaces is that water droplets bead on them with high contact angles (up to 179°) so that the droplets are very nearly spherical¹⁻³. These contact angles are much higher than those obtained by purely chemical surface treatments which achieve maximum contact angles of about 130° . Nearly spherical droplets roll very easily when the surface is tilted or moved. It is believed that lotus leaves (which have a superhydrophobic surface) take advantage of this effect to be self-cleaning³. The rolling droplets pick up dust and dirt particles as they roll off of the leaf.

The ease with which water droplets move on superhydrophobic surfaces prompted researchers to consider if such surfaces might also reduce drag in pipe and channel flow. Early experiments⁴⁻⁸ suggested that they did indeed reduce drag in both laminar and turbulent boundary layer flows. However, the reasons for this apparent drag reduction were not clear, as the mechanisms at work in droplet motion can not be present in these flows. Leading and trailing contact angles certainly have no role in channel or pipe flow. The explanation for superhydrophobic drag reduction in laminar channels was first demonstrated in Ou *et al.*⁹. In short, it was shown that air trapped in the microscale features is responsible for drag reduction. For a normal hydrophilic surface, capillary (surface tension) forces would quickly drive air out of the small surface cavities (as occurs in a sponge or cloth). However, because the surface is also chemically

hydrophobic, the water resists being drawn into the microcavities. As a result, superhydrophobic surfaces trap air at their surface and may even be able to remove dissolved air from the water solution. Beyond its role in allowing air cavities to form, chemical hydrophobicity has little or no effect on the subsequent drag reduction. Drag reduction results from the fact that water can slip over the air cavity surface, whereas it comes to rest on a flat solid surface, hydrophobic or not.

The amount of drag reduction in laminar flows is primarily a function of the size of the air cavities; increasing the fraction of air on the surface or increasing the spacing of the features increases the slip and the drag reduction^{9,10}. The maximum size of the air cavities is limited by the fact that air-water interfaces bridging very large cavities can fail. This occurs when the pressure becomes large enough to overwhelm the surface tension forces supporting the cavity or when gravitational, shear, or other dynamic instabilities are strong enough to rupture the air cavity's free surface. Subsequent research efforts¹⁰⁻¹² have confirmed this model of laminar drag reduction due to superhydrophobic surfaces. In the case of roughness composed of regularly spaced ridges an analytical solution corresponding to this model exists¹³⁻¹⁵ and experimental results appear to agree well with this solution^{9,10}, specifically velocity profiles above the no-slip and shear-free regions of the surfaces discussed in Philip^{13,14} and Lauga¹⁵.

Most research on superhydrophobic surfaces currently involves very regular surface geometries - often regularly spaced ridges or posts. These surfaces tend to be used in research as they allow very precise characterization of the topology. The model suggests that surface topology is the primary factor in the resultant drag reduction thus it is important to characterize. This paper will continue in the tradition of using simple, easily characterized surfaces, but it should be noted that in practice

unstructured surface roughness works just as well, and is often easier to fabricate. Some early experiments¹⁶ used plasma etched polypropylene which produces a random surface that achieved up to 25% drag reduction. More recent experiments have used hydrophobically treated sand paper¹⁷.

The use of superhydrophobic surfaces to produce laminar drag reduction in boundary layers is interesting since, at millimeter scales, no other drag reduction process is known. At nano-scales, chemical slip is possible and electrostatic effects are possible. On the other hand, for turbulent boundary layer flows there are numerous and quite varied ways to achieve drag reduction. These include fluid additives such as polymers and air bubbles¹⁸, surface modifications such as riblets¹⁹, compliant coatings²⁰, and active control techniques. Work by Tyrrell and Attard²¹ investigated the role of nano-bubbles trapped in hydrophobic surfaces and their relation to drag reduction. However, given the huge variety of different kinds of turbulent boundary layer applications, it is of interest to also understand the drag reducing properties and controlling mechanisms of superhydrophobic surfaces on turbulent boundary layers.

In a typical boundary layer, surface roughness enhances the turbulence levels and the drag. It is therefore not entirely obvious that superhydrophobic surfaces (and their associated surface roughness) will necessarily reduce drag in a turbulent boundary layer. Nevertheless, early experiments^{4,8} indicated that drag reduction does occur when using superhydrophobic surfaces even for turbulent flows. More recent experiments^{22,23} have confirmed this. A theoretical analysis by Fukugata²⁴ proposes an explanation of how a small alteration of the laminar sublayer can affect the entire turbulent boundary layer and subsequently alter the drag.

Perhaps the earliest computational study of these surfaces was performed by Min and Kim^{25,26}. This was a turbulent channel flow simulation in which an assumed slip boundary condition was applied and drag reduction was observed. The slip boundary condition is an effective (macroscopic) boundary condition, not a physical one, so these simulations correspond to the situation where the spacing of the surface roughness elements is much smaller than any turbulent eddies. Martell *et al.*²⁷ performed direct numerical simulations in which the topology was fully resolved at a single Reynolds number $Re_\tau \approx 180$. This means that no-slip boundary conditions were imposed on the roughness elements (posts or ridges) and a pure slip (no stress) boundary condition was imposed at the air cavity interface. The effective macroscopic slip of the surfaces was then calculated from the simulation, not imposed by it. The simulations in our previous work²⁷ had a roughness feature spacing that was of a size comparable to the energetic near-wall vortex size and streak spacing.

In Martell, *et al.*²⁷ the effects of superhydrophobic surface spacing and geometry were studied at a single turbulent Reynolds number. An increase in slip velocity

and drag reduction with increasing feature spacing and increased free surface area were observed. The Reynolds stresses showed a marked shift with the presence of a superhydrophobic surface. R_{11} , R_{22} , and R_{33} curves peaked lower and closer to the superhydrophobic surface than their smooth channel counterpart. The shear stress R_{12} shifted toward the superhydrophobic wall. This paper is a continuation of Martell, *et al.*²⁷ that explores the effect of Reynolds number on superhydrophobic surface performance, as well as the effect of larger roughness spacing, and the underlying physical processes responsible for the turbulent boundary layer drag reduction.

II. COMPUTATIONAL APPROACH

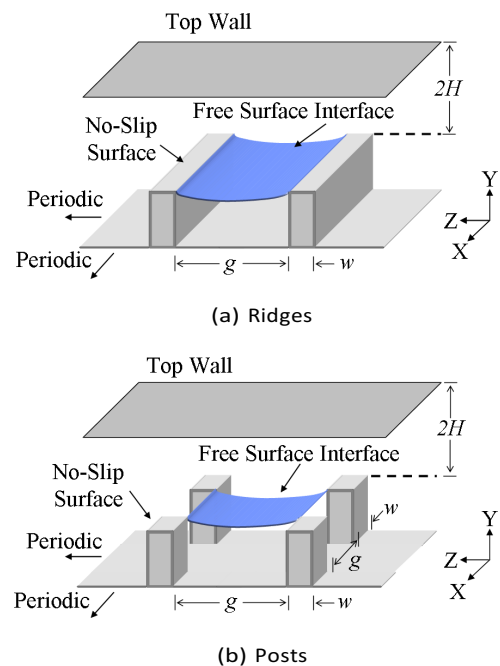


FIG. 1. Schematic of geometry and relevant dimensions for superhydrophobic surface features. Note that in the simulations, the air-water interface is flat.

The two roughness configurations considered in this work are shown in Figure 1. In both configurations turbulent channel flow with a constant pressure gradient is simulated. The flow has periodic boundary conditions applied in the streamwise (X) and spanwise (Z) directions. A regular, no-slip wall is applied at the top of the channel, and regions of no-slip (on the top of the ridge or post) and pure slip flow (on the air cavity interface) are applied on the superhydrophobic lower wall. Only the water side of the air cavity is simulated, and the free surface between the posts or ridges is assumed to be perfectly flat. Recent work by Ybert *et al.*²⁸ suggests that curvature effects exist, but have a negligible effect on the drag under modest static pressures. Estimates based on

the maximum possible deflection angle of 12° ²⁹ also suggest curvature is a secondary influence. The assumption of a pure slip surface at the air interface is reasonable if the roughness features are tall enough (i.e. the same order of magnitude as the spacing). Very thin air cavities could lead to shear flow in the air cavities and a deviation from the slip boundary condition at the air cavity free surface.

The dimensionless length of the channel was $L_x/H = 6$ where H is the channel half height. The width was $L_z/H = 3$. This is roughly equivalent to the values of 2π and π that were found to be sufficient for prior spectral simulations of channel flow³⁰. The simulations do not require dimensions, but for comparison with experiments we note that if the working fluid was water (at 20°C), these computations correspond to a channel half height H on the order of 0.15 mm if the post or ridge sizes are assumed to be $30\mu\text{m}$ across (which is a common size found in experiments^{22,31}). A total of 13 cases were simulated. They are described in Table I. At higher Reynolds numbers this study looks at equally spaced ridges (50% free surface area), and widely spaced posts (93.75% free surface area). In addition, a case with evenly spaced ridges perpendicular to the flow direction at $Re_\tau \approx 180$, referred to as transverse ridges, was investigated.

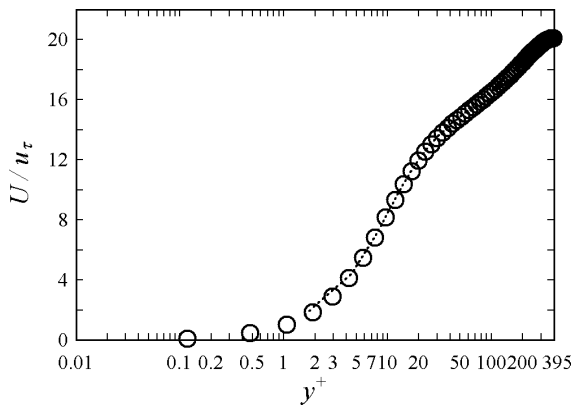


FIG. 2. $Re_\tau \approx 395$: A comparison of near wall velocity profiles obtained from Moser *et al.*³⁰ () and the CFD code (·) for turbulent channel flow between two infinite parallel plates.

The $Re_\tau \approx 180$ cases use 128^3 grid points for each simulation. The $Re_\tau \approx 395$ cases require 256^3 grid points, and the $Re_\tau \approx 590$ cases use 512^3 grid points per simulation. A uniform mesh is employed in all directions. Stretching in the wall normal direction is not required. The code uses a staggered mesh spatial discretization, low-storage third-order Runge-Kutta time advancement for the advection terms, trapezoidal advancement for the viscous terms, and a classic fractional step method for the pressure term and incompressibility constraint³². It is parallelized using MPI libraries and efficiently hides all inter-CPU data transfers by performing them asynchronously during the computations. The spatial dis-

cretization has no artificial dissipation associated with it³³ (which could alter the turbulent energy cascade³⁴). The numerical method locally conserves vorticity (or circulation), as well as mass and momentum, to machine precision³⁵.

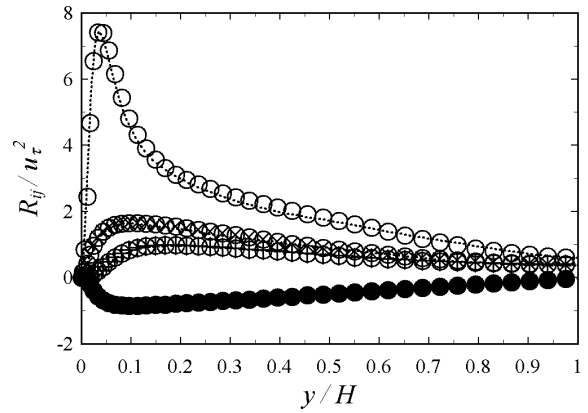


FIG. 3. $Re_\tau \approx 395$: A comparison of Reynolds stress profiles obtained from Moser *et al.*³⁰ (R_{11} , $\oplus R_{22}$, $\otimes R_{33}$, $\bullet R_{12}$) and the CFD code (· · ·) for turbulent channel flow between two infinite parallel plates.

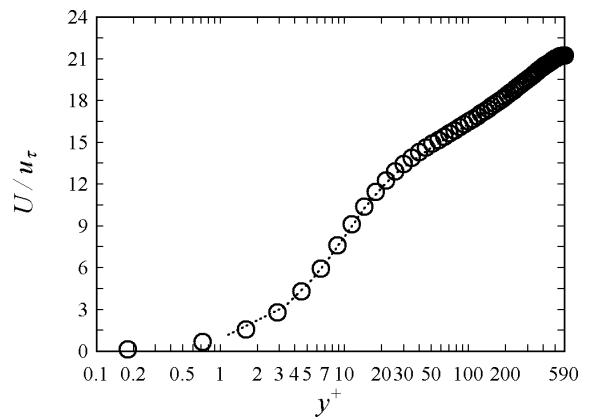


FIG. 4. $Re_\tau \approx 590$: A comparison of near wall velocity profiles obtained from Moser *et al.*³⁰ and the CFD code (see Figure 2 for symbol key).

The code has been extensively tested^{27,29,36,37}. It was validated for laminar superhydrophobic surface calculation and turbulent superhydrophobic surfaces at $Re_\tau \approx 180$ in Martell, *et al.*²⁷. Validation of the turbulence simulation capabilities of the code against the higher Reynolds number standard channel flow simulations of Moser *et al.*³⁰ are shown in Figures 2 through 5. These figures show the mean flow and Reynolds stresses that are computed when the bottom wall is a regular no-slip wall. Only half of the domain is shown since the statistics are symmetric for this particular case. The mean flow

matches to within 2% and the Reynolds stresses match to within 5%. The greatest difference is in the stream-wise Reynolds stress in the core of the channel. Stream-wise and spanwise velocity correlations were also calculated for all three regular no-slip wall benchmark cases ($Re_\tau \approx 180$, $Re_\tau \approx 395$, and $Re_\tau \approx 590$). Correlations approached zero as the edge of the computational domain was reached, and generally agreed with correlation data provided by Moser *et al.*³⁰, although temporal averaging was not employed. Correlation data for the regular wall $Re_\tau \approx 395$ case is compared with streamwise and spanwise velocity correlations from a case with widely spaced posts in Section V, Figures 39 and 40. These figures show that the size of the computational domain is sufficient not only for a regular wall channel but also when significant slip is present on the bottom wall. This is discussed further in Section V. In addition to comparisons with Moser *et al.*³⁰, a mesh resolution study was performed. This simulation involved evenly spaced ridges (with $g/w = 1$) at $Re_\tau \approx 180$. This simulation was run with both 128^3 and 256^3 meshes. The Reynolds stresses were all within 3% of each other, and the mean velocity profiles differ by less than 0.5% of the bulk velocity.

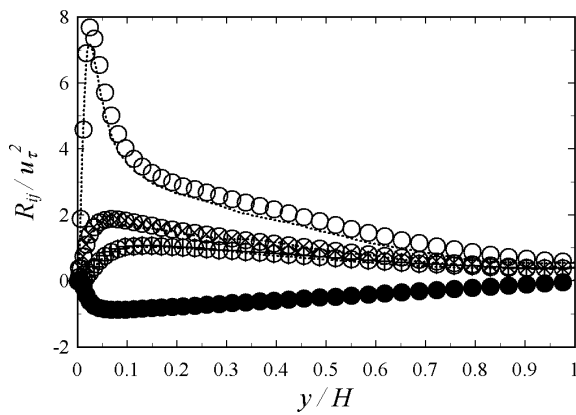


FIG. 5. $Re_\tau \approx 590$: A comparison of Reynolds stress profiles obtained from Moser *et al.*³⁰. See Figure 3 for symbol key.

III. MEAN FLOW

In the case of the ridge topology, the ridges are always aligned with the mean flow (except in the special case of transverse ridges), thus the turbulent statistics depend on both the distance from the surface (Y) and the spanwise location (Z) (transverse ridges are dependent upon X and Y). The turbulent statistics just above a ridge are different from those just above a free surface region. For the post geometry, the statistics are also dependent on the streamwise location (X). For this reason, the statistics are calculated by temporal averaging and ensemble averaging over all the posts or ridges on the surface. In

practice, the topological surface features are very small (on the scale of microns), and engineers are interested in the larger scale bulk properties of the flow. In this paper, we present the X - Z planar averaged mean flow and Reynolds stress profiles as a function of the distance to the wall (Y). The distinction between the planar averaged statistics and the actual turbulent statistics is only important at distances to the wall that are less than the gap width. However, in that region this distinction is critical. Using the planar averaged mean velocity rather than the actual (spatially varying) mean velocity to calculate the Reynolds stresses produces erroneous results. This may be a particular issue in experimental studies where the spatially varying mean flow is very difficult to measure.

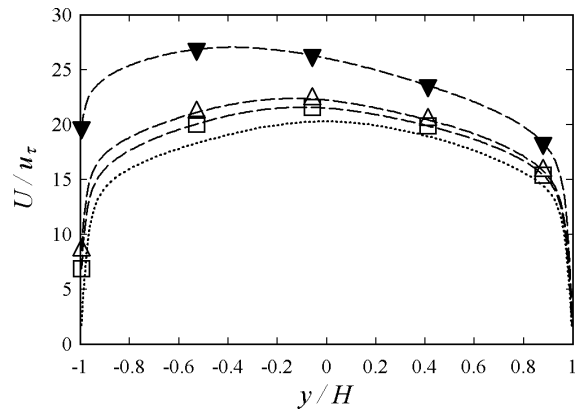


FIG. 6. $Re_\tau \approx 395$: Velocity profiles from simulations with $w^+ = g^+ = 37.031$ (Q) and $w^+ = g^+ = 74.062$ (A) ridges, as well as $w^+ = 37.031$, $g^+ = 111.09$ (V) posts. Regular channel profile (· · ·) shown for reference. Note that symbols are used to identify curves, and do not reflect data point locations.

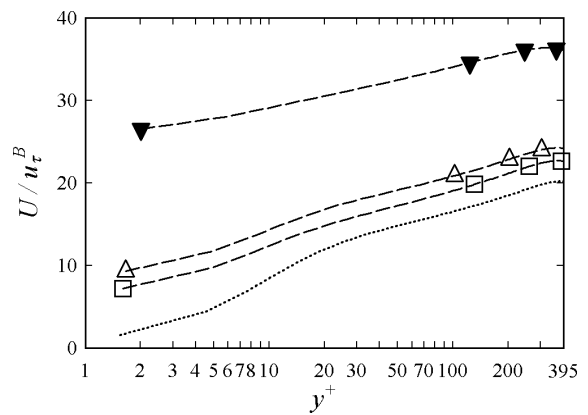


FIG. 7. $Re_\tau \approx 395$: A closer look at velocity profiles from Figure 6, using the local friction velocity, u_τ^B to normalize the velocity and calculate y^+ .

TABLE I. Reynolds numbers, line types, geometric ratios, and length scales for the cases investigated. Note that most $Re_\tau \approx 180$ cases are presented in Martell, *et al.*²⁷.

Re_τ	Line type	Geometry	g/w	w/H	g/H	w^+	g^+
180	---	Ridges	1.0	0.09375	0.09375	16.875	16.875
			1.0	0.18750	0.18750	33.750	33.750
			1.6	0.14062	0.23436	25.312	42.187
			3.0	0.09375	0.28124	16.875	50.625
		Posts	1.0	0.18750	0.18750	33.750	33.750
			1.6	0.14062	0.23436	25.312	42.187
			3.0	0.09375	0.28124	16.875	50.625
			1.0	0.18750	0.18750	33.750	33.750
395	---	Ridges	1.0	0.09375	0.09375	37.031	37.031
			1.0	0.18750	0.18750	74.062	74.062
		Posts	3.0	0.09375	0.28124	37.031	111.09
			1.0	0.18750	0.18750	110.62	110.62
590	-..-	Ridges	1.0	0.18750	0.18750	110.62	110.62
		Posts	3.0	0.09375	0.28124	55.313	165.94

Two different ridge geometries and one post geometry were studied at $Re_\tau \approx 395$. The planar averaged mean velocity profiles for those three cases as well as standard channel flow are shown in Figure 6. Spencer, *et al.*³⁸ saw similar shifts in peak velocity toward a hydrophobic wall in their investigations. The post case, with its larger gap size (and much larger free surface area percentage) shows the most slip on the lower wall and the greatest mass flux. Because these simulations have the same Re_τ they are effectively operating at the same pressure gradient. This shows that with a superhydrophobic surface, more mass can be moved through the channel for the same effort. To show that the slip is actually a function of the gap spacing (and not simply the free surface area percentage), the two ridge cases have exactly the same free surface area percentage and different gap spacings. The smaller gap size (Q) results in a smaller slip velocity on the lower wall and less mass flux. To first order, it can be seen that the additional mass flux produced by a superhydrophobic surface is roughly proportional to the gap size of that surface. For this reason, very small (nano-scale) features may be ineffective for drag reduction. Figure 7 shows the velocity profiles in wall units (based on the bottom wall). The effective slip velocity caused by the superhydrophobic surfaces is now quite apparent. To first order these surfaces shift the log-law upwards, but do not alter its slope.

The behavior of the mean flow as the Reynolds number increases to $Re_\tau \approx 590$ is shown in Figure 8. The same profile in wall units based on the superhydrophobic (bottom wall) friction velocity is shown in Figure 9. Again, in this case, higher Reynolds number essentially implies that a higher pressure gradient is being applied to the same channel. As expected, this drives the fluid faster through the channel. The slip velocity, however, does not appear to be a strong function of the Reynolds number. This can be seen clearly in Figure 16, when the slip velocity is normalized by the average velocity in the

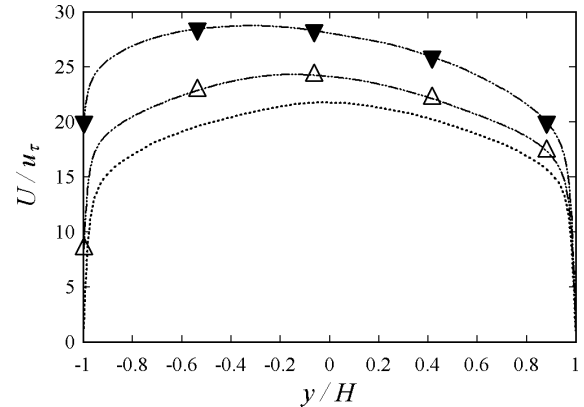


FIG. 8. $Re_\tau \approx 590$: Velocity profiles from simulations with $w^+ = g^+ = 110.62$ (Δ ridges, as well as $w^+ = 55.313$, $g^+ = 165.94$ (∇) posts. Regular channel profile (\cdot) shown for reference. Note that symbols are used to identify curves, and do not reflect data point locations.

channel. As will be discussed later, it is possible that the $Re_\tau \approx 180$ case is showing low Reynolds number effects and the two higher Reynolds number cases are more indicative of fully developed channel flow.

The velocity profiles for evenly spaced ridges at varying Reynolds numbers are shown in Figure 10. The velocity in locally scaled wall units is shown in Figure 11. The mean flow profiles for widely spaced posts at varying Reynolds numbers are shown in Figure 12, while the velocity in locally scaled wall units is shown in Figure 13. For both posts and ridges, the slip velocity is only mildly dependent on the Reynolds number for the higher Reynolds number cases. In the case of transverse ridges, it is not surprising that they admit a very small slip velocity at the superhydrophobic wall as seen in Figures 14 and 15. The amount of slip admitted by transverse

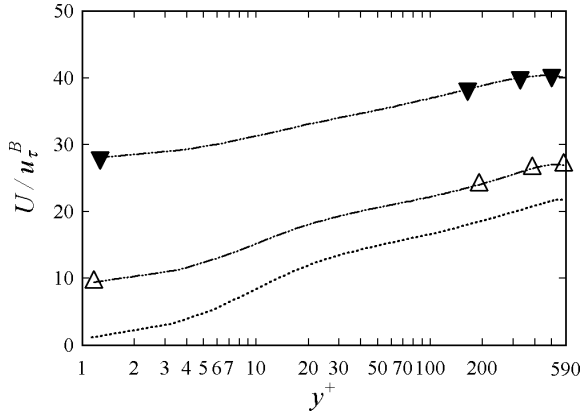


FIG. 9. $Re_\tau \approx 590$: A closer look at velocity profiles from Figure 8, using the local friction velocity u_τ^B to normalize the velocity and calculate y^+ .

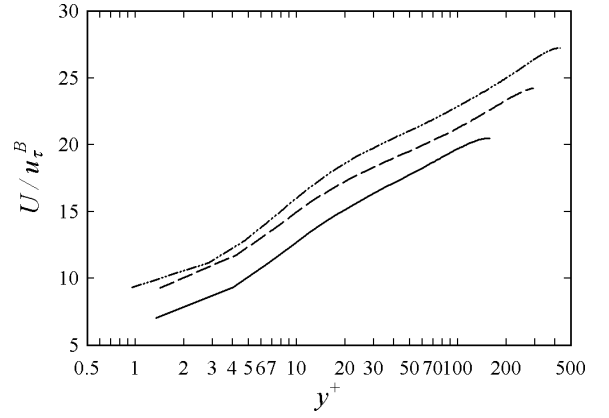


FIG. 11. A closer look at velocity profiles from Figure 10, using the local friction velocity u_τ^B to normalize the velocity and calculate y^+ .

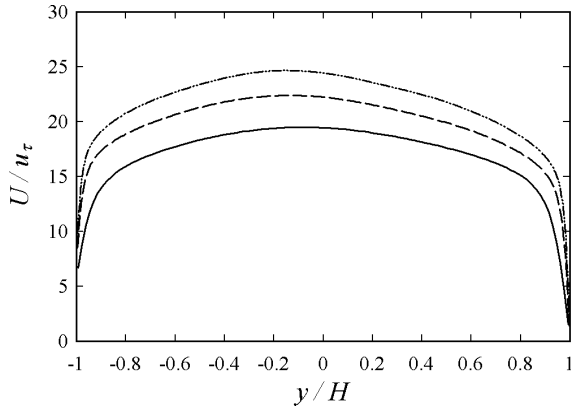


FIG. 10. Comparison of velocity profiles for $g/w = 1$, $w/H = g/H = 0.1875$ ridges across the three Reynolds numbers investigated: $Re_\tau \approx 180$ (—) with $w^+ = g^+ = 33.75$, $Re_\tau \approx 395$ (---) with $w^+ = g^+ = 74.062$, and $Re_\tau \approx 590$ (- · -) with $w^+ = g^+ = 110.62$.

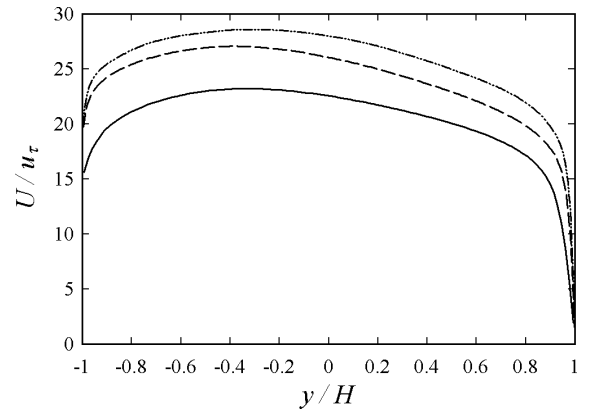


FIG. 12. Comparison of velocity profiles for $g/w = 3$, $w/H = 0.09375$, $g/H = 0.28124$ posts across the three Reynolds numbers investigated: $Re_\tau \approx 180$ (—) with $w^+ = 16.875$, $g^+ = 50.625$; $Re_\tau \approx 395$ (---) with $w^+ = 37.031$, $g^+ = 111.09$; and $Re_\tau \approx 590$ (- · -) with $w^+ = 55.313$, $g^+ = 165.94$.

ridges may be reduced further if the interface were allowed to deflect, as this may lead to recirculation above the ridge gaps. Recirculation, along with streamline curvature, might affect a drag *increase* similar to what was shown in Min and Kim's work²⁵ when transverse slip was considered. The slip velocity as a percentage of the bulk velocity versus the Reynolds number is shown in Figure 16 for both the ridge and post cases. This figure confirms that the Reynolds number is not a strong factor in the observed dimensionless slip velocity of the superhydrophobic surface. This is important because it is likely that these surfaces will be used at much higher Reynolds numbers than we have computed here. The effective slip is an important parameter because it is directly related to the drag reduction. In our simulations, the pressure gradient is fixed, so that reduced drag on the superhydro-

phobic wall will lead to increased drag on the upper wall (because of the increased mass flow) and the same total drag in the channel. Figure 17 plots the slip velocity normalized by the bottom-wall friction velocity versus Reynolds number, and Figure 18 plots the drag reduction on the lower wall versus the Reynolds number (for the ridge and post cases). These figures show that the percent drag reduction varies with Reynolds number. It is important to note that increasing the Reynolds number while keeping g/H and w/H fixed increases the microfeature spacing in wall units (w^+ and g^+). Thus even though all of the simulations in Figures 10 through 18 are performed at the same physical post or ridge width and spacing, their dimensions in wall units increases substantially with increasing Reynolds number. Transverse

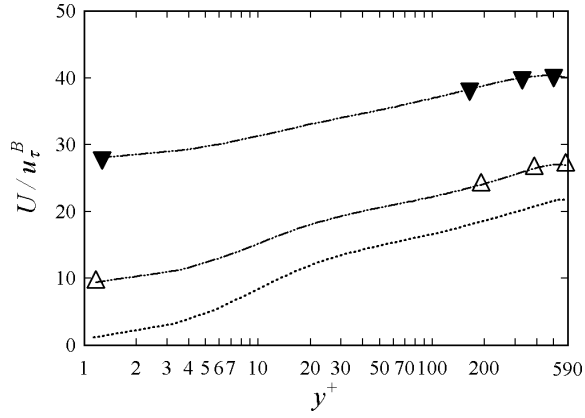


FIG. 13. A closer look at velocity profiles from Figure 12, using the local friction velocity u_τ^B to normalize the velocity and calculate y^+ .

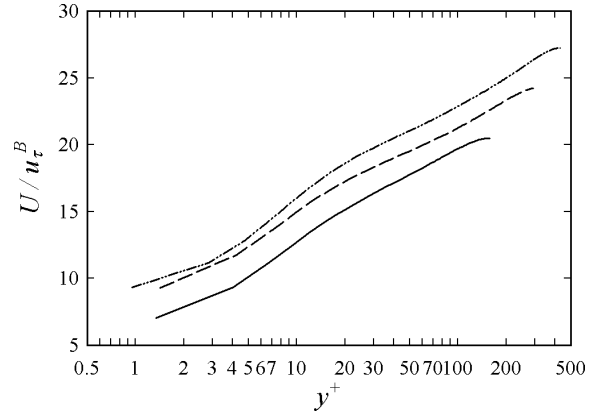


FIG. 15. A closer look at velocity profiles from Figure 14, using the local friction velocity u_τ^B to normalize the velocity and calculate y^+ .

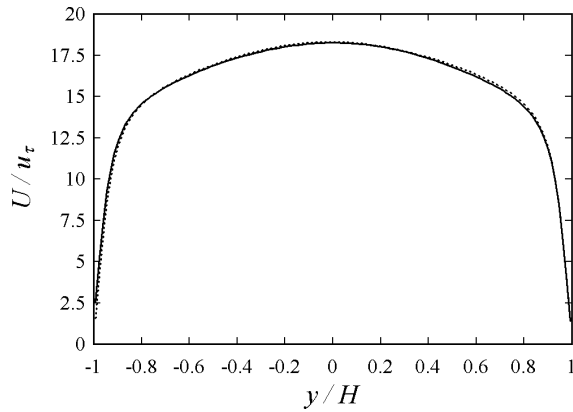


FIG. 14. Comparison of velocity profiles for transverse $g/w = 1$, $w/H = g/H = 0.18750$ ridges at $Re_\tau \approx 180$ (—) with regular channel profile (···) shown for reference.

ridges exhibit negligible shear stress reduction and closely resemble the regular channel results. This adds further evidence that feature spacing, and perhaps feature alignment, play a key role in surface performance. We hypothesize that feature spacing in wall units, and not Reynolds number, is the critical criteria for characterizing superhydrophobic performance in turbulent flows. To test this hypothesis, two ridge geometries were simulated at different physical spacings and Reynolds numbers, but with nearly identical ridge spacing and width in wall units. The velocity profiles from these two simulations are shown in Figure 19. When normalized by the friction velocity, the profiles collapse. Thus neither increasing the Reynolds number or reducing the physical gap size had an effect on the performance of the superhydrophobic surface. This confirms our hypothesis that it is the gap spacing in wall units that dictates drag reduction. This suggests that it might be more appropriate to

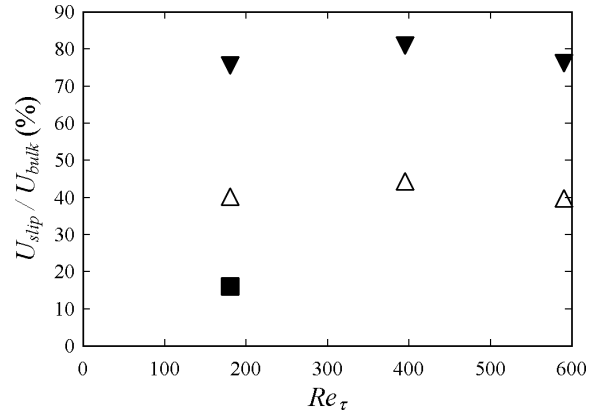


FIG. 16. Slip velocity as a percentage of bulk velocity for $g/w = 1$, $w/H = g/H = 0.18750$ ridges (Δ) and $g/w = 3$, $w/H = 0.09375$, $g/H = 0.28124$ posts (∇) at $Re_\tau \approx 180, 395$, and 590 , as well as transverse $g/w = 1$, $w/H = g/H = 0.18750$ ridges (\square). Note that the ridge spacing in wall units increases with increased Re_τ .

plot drag reduction as a function of the feature spacing in wall units w^+ rather than as a function of Reynolds number. Figure 20 shows superhydrophobic surface shear stress reduction as a function of g^+ for fixed $w^+/g^+ = 1$. A nearly linear growth in drag reduction is observed for both the superhydrophobic ridges and posts. A deviation from this trend will likely be observed at low values of feature spacing if the value of drag reduction in laminar flow is to be recovered. Note that τ_w is the wall shear stress present in a comparable regular wall channel.

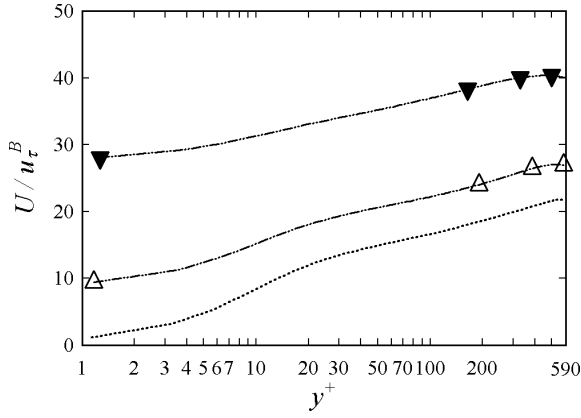


FIG. 17. Slip velocity normalized by bottom-wall friction velocity for the same geometries shown in Figure 16.

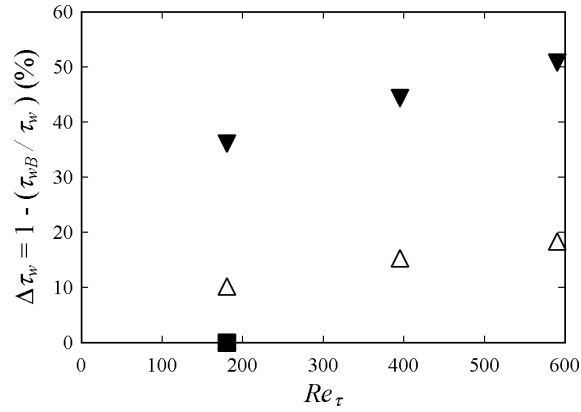


FIG. 18. Superhydrophobic surface shear stress reduction as a function of friction Reynolds number for the same geometries and Reynolds numbers reported in Figure 16.

IV. REYNOLDS STRESSES

Figures 21 through 24 show the normalized planar averaged Reynolds stresses for all the cases at $Re_\tau = 395$. The results suggest that mean shear is still the primary influence on the turbulence levels. Reduced shear at the superhydrophobic surface results in reduced turbulent production and lower turbulence levels for all the shear stresses. The magnitude of the turbulence drop is closely related to the magnitude of the shear reduction that occurred due to the slip on the surface. Similarly, on the regular (upper) wall the shear increases (due to the additional mass flow through the channel) and the turbulence levels increase accordingly. Note that all Reynolds stresses are scaled by the square of the friction velocity u_τ^2 which is the average of the top and bottom wall friction velocities.

The variation as the Reynolds number increases to

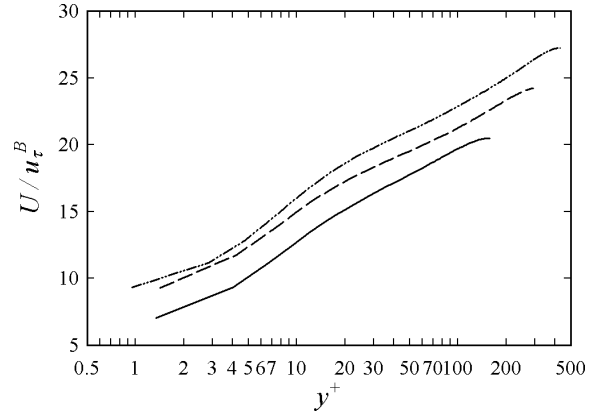


FIG. 19. Near-wall velocity profiles for $w^+ = g^+ = 33.75$ ridges ($w/H = g/H = 0.1875$) at $Re_\tau \approx 180$ (—) and $w^+ = g^+ = 37.031$ ridges ($w/H = g/H = 0.09375$) at $Re_\tau = 395$ (---). The profiles lie atop one another, indicating the increase in Reynolds number may not affect the superhydrophobic surface performance.

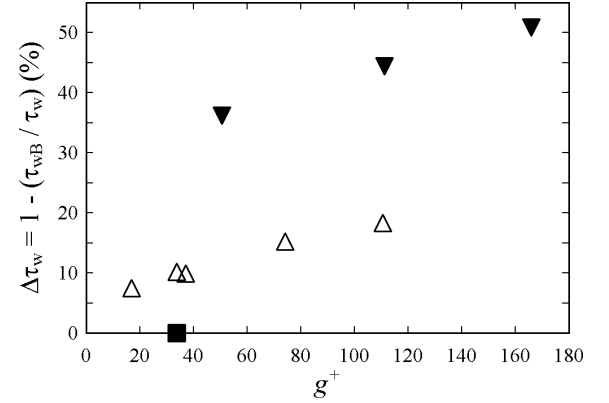


FIG. 20. Superhydrophobic surface shear stress reduction as a function of g^+ for fixed $w^+/g^+ = 1$ ridges (Δ), posts (∇), and transverse ridges (\square). Transverse ridges exhibit near-zero shear stress reduction.

$Re_\tau = 590$ is shown in Figures 25 through 28 for both the widely spaced posts and evenly spaced ridges. At higher Reynolds numbers, the high-shear region lies closer to the wall and is stronger. This was also observed by Spencer, *et al.*³⁸ who saw similar changes in Reynolds stress profiles near hydrophobic walls. This is reflected in the turbulence intensities. For a given surface topology (in w/H and g/H) the peak turbulence levels increase with Reynolds number and move toward the wall. When comparing the different surface topologies against each other, it is clear that the posts reduce the normal fluctuation (R_{22}) more than the ridges do, and the posts enhance the surface parallel fluctuations (R_{11} and R_{33}) compared to the ridges. The enhanced wall parallel fluctuation

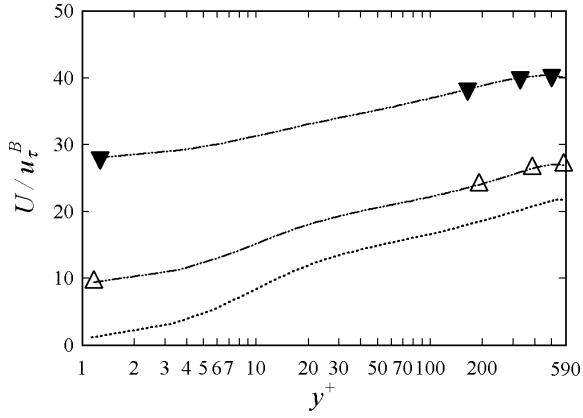


FIG. 21. $Re_\tau \approx 395$: R_{11} profiles from simulations with $w^+ = g^+ = 37.031$ (Q) and $w^+ = g^+ = 74.062$ (A) ridges, as well as $w^+ = 37.031$, $g^+ = 111.09$ (V) posts. Regular channel profile ($\cdot\cdot\cdot$) shown for reference. Note that symbols are used to identify curves, and do not reflect data point locations.

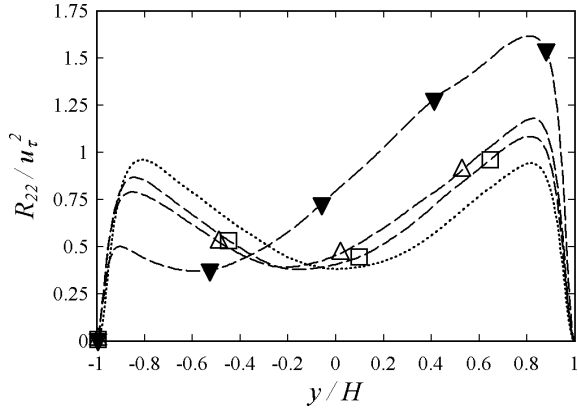


FIG. 22. $Re_\tau \approx 395$: R_{22} profiles for the same geometries reported in Figure 21.

tuations are a result of the extensive free surface area (93.75%) provided by the posts (versus the 50% free surface coverage found in the ridge case). A free surface does not damp surface-parallel fluctuations and a solid wall does³⁹. While the superhydrophobic surface reduces the mean shear and hence the turbulent production, it also significantly reduces the amount of energy dissipation near the surface (by removing the surface-parallel viscous damping of the turbulence). For this reason, the flow does not relaminarize on the superhydrophobic surface when local shear arguments alone might suggest it should. Note that the unsmooth regions present in the $Re_\tau 590$ post Reynolds stress profiles are a result of insufficient statistical averaging in time and are not indicative of any physical phenomena. It is of no surprise that the Reynolds stress profiles for transverse ridges are nearly identical to those for the regular channel as seen

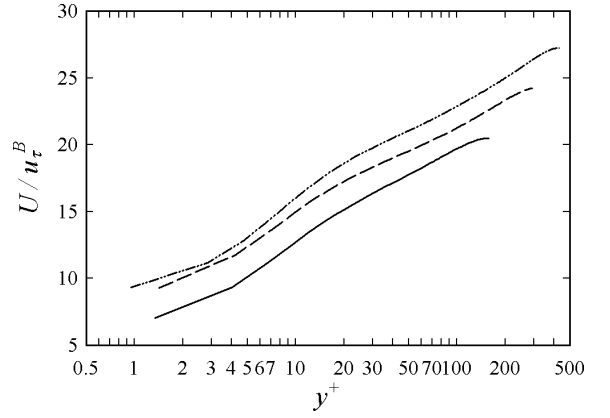


FIG. 23. $Re_\tau \approx 395$: R_{33} profiles for the same geometries reported in Figure 21.

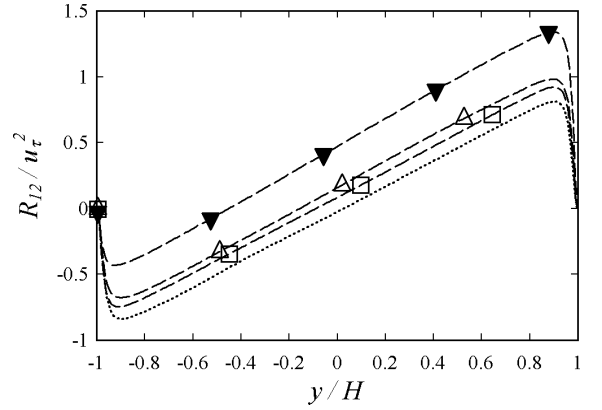


FIG. 24. $Re_\tau \approx 395$: R_{12} profiles for the same geometries reported in Figure 21.

in Figures 29 and 30. Unlike their streamwise counterparts, the transverse ridges do not appear to affect the location or intensity of turbulent structures in the flow.

The Reynolds stresses are plotted in wall coordinates in Figures 31 through 34 for $g/w = 1$, $w/H = g/H = 0.18750$ ridges at $Re_\tau \approx 180$, $Re_\tau \approx 395$, and $Re_\tau \approx 590$. The local (lower wall) friction velocity is used in the normalization and in the calculation of y^+ . While these figures appear to show Reynolds number variation, it is hypothesized that they may be revealing variation with gap and feature widths g^+ and w^+ .

V. STRUCTURES

The mean flow profiles and Reynolds stresses imply that the superhydrophobic surface does not alter the fundamental structures of the turbulent boundary layer. The near wall behavior of the turbulent shear stress (R_{12})

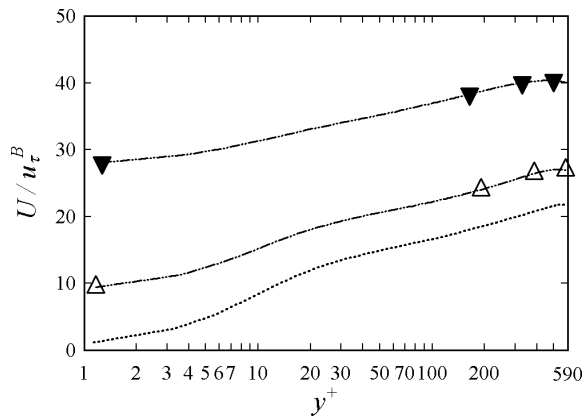


FIG. 25. $Re_\tau \approx 590$: R_{11} profiles from simulations with $w^+ = g^+ = 110.62$ (Δ) ridges, as well as $w^+ = 55.313$, $g^+ = 165.94$ (∇) posts. Regular channel profile (\cdots) shown for reference.

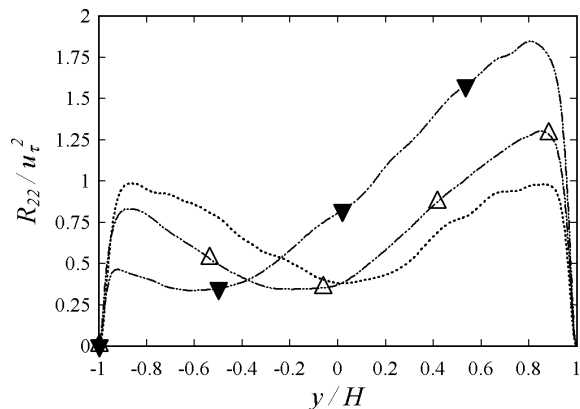


FIG. 26. $Re_\tau \approx 590$: R_{22} profiles for the same geometries reported in Figure 25.

continues to collapse on wall shear units. The log-law remains intact (though shifted upwards) for the mean flow. This section will look closely at the streaks (and streamwise vortices) associated with boundary layer flows, and will investigate how they are affected by the regular array of microfeatures on the superhydrophobic surface.

Streaks (pairs of counter-rotating vortices) have an average spanwise spacing of roughly 100^+ units⁴⁰. This means that as the Reynolds number is increased (w/H and g/H are held fixed), the streaks (and their associated streamwise vortices) become smaller. Figure 35(a) depicts the size and shape of vortices for a channel with evenly spaced ridges ($w/H = 0.125$) at $Re_\tau \approx 180$ on a cross section looking down the channel. The tops of the ridges are shown with a solid black line and the tops of each free surface are shown with a dashed line. The counter-rotating streamwise vortices that form the low-speed and high-speed streaks are shown residing just

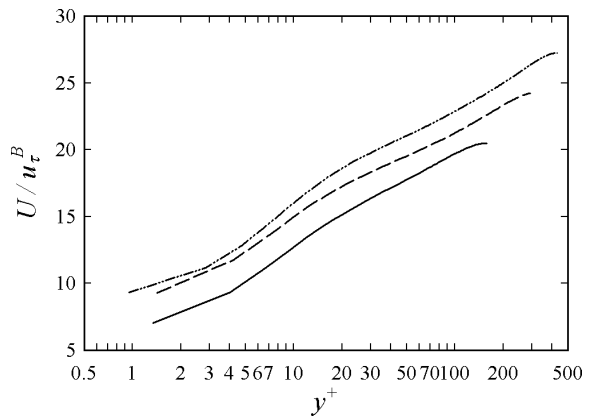


FIG. 27. $Re_\tau \approx 395$: R_{33} profiles for the same geometries reported in Figure 25.

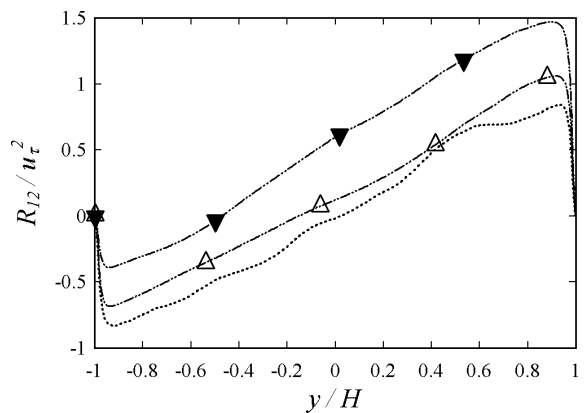


FIG. 28. $Re_\tau \approx 590$: R_{12} profiles for the same geometries reported in Figure 25.

above the surface. For this particular case, the ridge spacing and the streak spacing are nearly equal. Having the ridge spacing equal to the streak spacing means that the ridges have the potential to act like riblets (see Choi, *et al.*⁴¹). Riblets reduce drag by damping the spanwise motion of streamwise vortices. This could be a reason (in addition to low Reynolds number effects) why the $Re_\tau \approx 180$ simulations behave slightly differently from the higher Reynolds number simulations. We note however, that the posts have little ability to control spanwise streak motion yet they too show slight differences at $Re_\tau \approx 180$.

Figure 35(b) shows the same surface topology at the higher Reynolds number, $Re_\tau \approx 590$. The vortices are now much smaller than the ridges and free surface regions (gaps), and the vortices are also closer to the superhydrophobic surface. It is unlikely now that the streaks and ridges (or posts) are acting like riblets. The Min and Kim simulations²⁵, where a slip boundary condition is assumed for the whole lower surface, would be equivalent

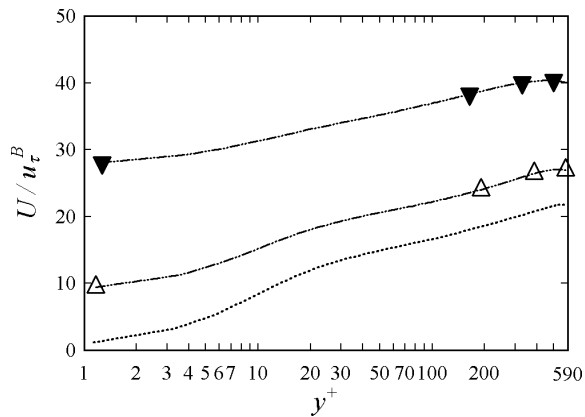


FIG. 29. $Re_\tau \approx 180$: R_{11} profiles from simulations with transverse $g/w = 1$, $w/H = g/H = 0.18750$ ridges (\square). Regular channel profile (\cdots) shown for reference.

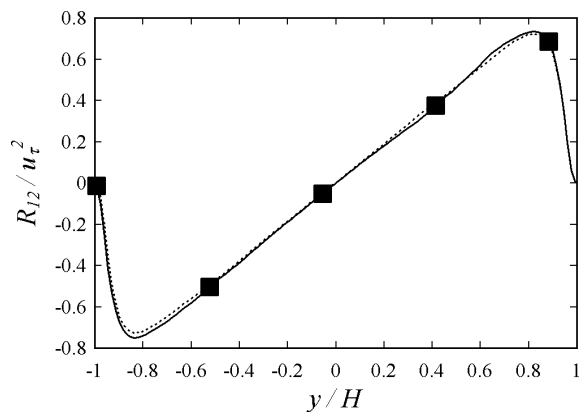


FIG. 30. $Re_\tau \approx 180$: R_{12} profiles for the same geometries reported in Figure 29.

to the opposite situation where the ridges are extremely small compared to the near wall structures.

The behavior of the mean flow and Reynolds stresses suggests that very similar near-surface structures are likely to exist adjacent to the superhydrophobic surface. This is confirmed by Figure 36 which shows a slice of the streamwise velocity, normalized by the bulk streamwise velocity, that is parallel to, and just above, the superhydrophobic surface, and Figure 37 which shows the vertical velocity (also normalized by the bulk streamwise velocity) in the same plane. The top picture is a regular channel flow (at $Re_\tau \approx 395$) and the bottom slice is from the widely spaced post case (at the same Reynolds number). The contour levels are identical in both pictures, so that it is clear that both the magnitude and size of the streaks are very similar in both flows. A bar corresponding to 50^+ wall units has been added to compare the relative sizes of features present in the flow. The slices are taken at y -positions where the local shear is

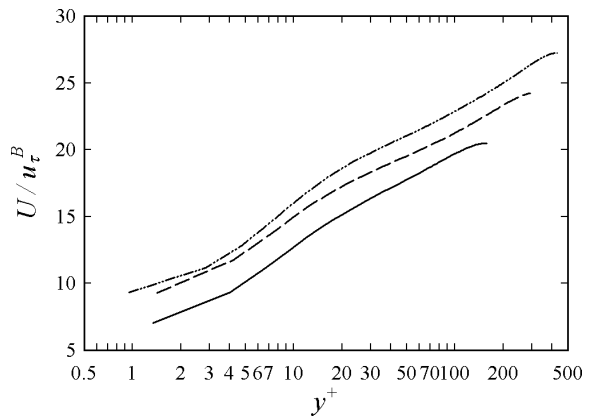


FIG. 31. Comparison of R_{11} profiles for $g/w = 1$, $w/H = g/H = 0.18750$ ridges across the three Reynolds numbers investigated: $Re_\tau \approx 180$ (—) with $w^+ = g^+ = 33.75$, $Re_\tau \approx 395$ (---) with $w^+ = g^+ = 74.062$, and $Re_\tau \approx 590$ (- · -) with $w^+ = g^+ = 110.62$.

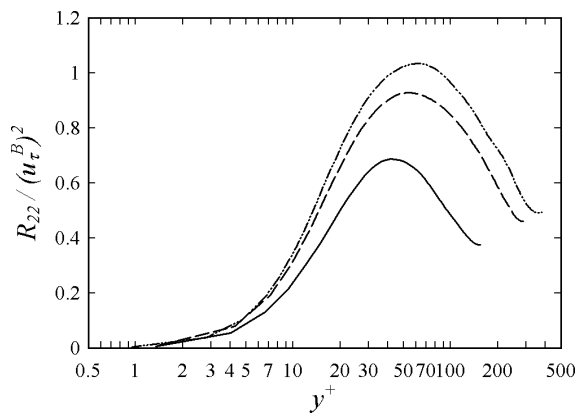


FIG. 32. Comparison of R_{22} profiles for the same cases discussed in Figure 31.

the same. In the case of the regular channel, the slice is at $y^+ \approx 44$ and in the case of the posts this level of shear does not occur until one is closer to the surface (at $y^+ \approx 22$). The location with the same mean shear was chosen because Lee, Kim, and Moin⁴² suggest that shear (not wall locality) is the driving mechanism in streak formation. The shift in position roughly corresponds to the slip-length in wall units. For the widely spaced post case in both Figures 36 and 37, the turbulent structures are not closely related to the post positions, although the structures shown in Figure 36(b) appear to remain aligned down the length of the channel while in (a), which shows the regular wall channel, the streaks intersect more and are generally less structured. The fact that the post case has only 6.25% of the surface occupied by a solid wall indicates that boundary layer turbulent structures are dominated by the mean shear and the zero vertical

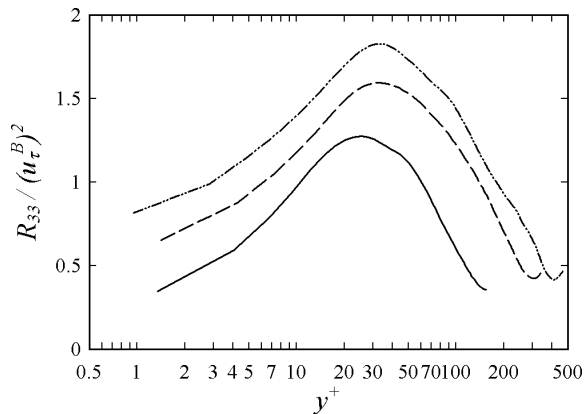


FIG. 33. Comparison of R_{33} profiles for the same cases discussed in Figure 31.

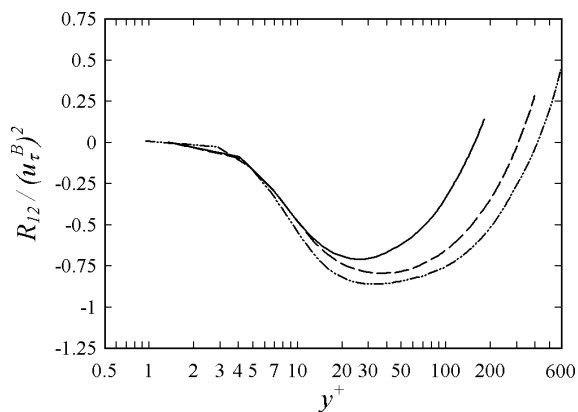


FIG. 34. Comparison of R_{12} profiles for the same cases discussed in Figure 34.

velocity (no penetration) boundary condition. The tangential boundary condition (slip or no-slip) appears to have a very significant affect on the overall drag without dramatically changing the nature of the near-wall turbulent structures. Note that the velocities are normalized by the bulk streamwise velocity in order to better accentuate the turbulent features present in the flow. The bottom wall friction velocity (u_τ^B) was *not* used for normalization as the value of u_τ^B differs greatly between regular channels and those with ridges or posts.

Figure 38 shows time-averaged streamwise velocity (U) contours over $w^+ = g^+ = 33.75$ streamwise ridges on the bottom wall at $Re_\tau \approx 180$. The difference between flow over the gaps (lighter regions with higher velocity) and flow over the ridges themselves (darker regions with near-zero velocity) is clearly seen. The presence of the ridges appears to affect the mean flow in the channel up to a height of $y^+ \approx 10 - 15$, and the smooth transition between shear-free and no-slip regions is observed. Statistics taken over the ridge will resemble those for a

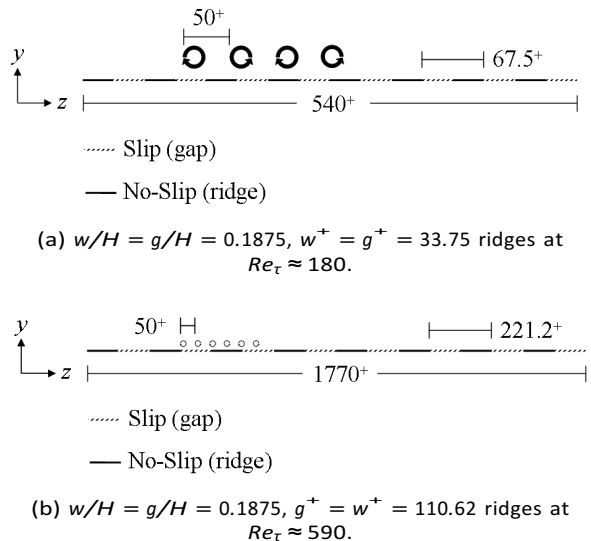


FIG. 35. Schematic representing pairs of counter-rotating vortices for channel flow over ridges at two different Reynolds numbers.

“normal” no-slip wall, and similarly statistics taken over a gap will be similar to those found above a “normal” free surface. Superhydrophobic features affect the near-wall region up to a distance less than or equal to the feature spacing in wall units (g^+).

Figures 39 and 40 compare velocity correlations in X and Z for a regular wall channel and $w^+ = 37.031$, $g^+ = 111.09$ post channel both at $Re_\tau \approx 395$. For the regular wall channel, correlations were calculated at $y^+ \approx 44$. For $w^+ = 37.031$, $g^+ = 111.09$ posts, correlations were computed at $y^+ \approx 22$. The correlations match well for moderate r_X and r_Z which further supports the hypothesis that shear may be primarily responsible for streak formation. Furthermore, the correlations show the computational domain is both wide and long enough even with significant shear free surface present on the lower wall. The unsmooth nature of the streamwise velocity correlation in the spanwise direction (seen in Figure 40) may be due to the presence of streaks and the lack of temporal averaging, as the behavior roughly corresponds to the spanwise streak spacing. Note that the size of the fluctuations does not correspond to the post size or spacing, and would most likely average to zero over time.

VI. CONCLUDING REMARKS

Superhydrophobic surfaces produce changes in turbulent channel flow through several different mechanisms. They allow average slip velocities (along the surface) which approach the channel’s bulk velocity. The shear stress at the superhydrophobic surface (which can be directly related to drag reduction) is significantly reduced

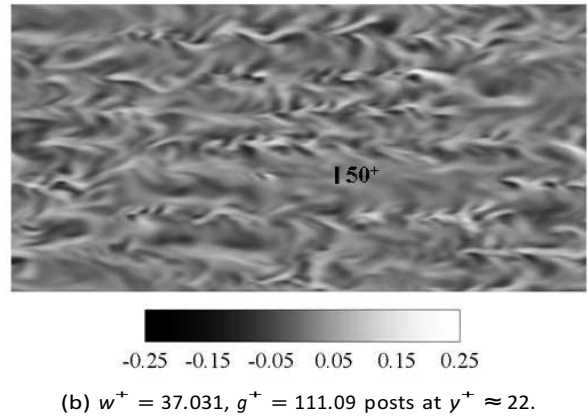
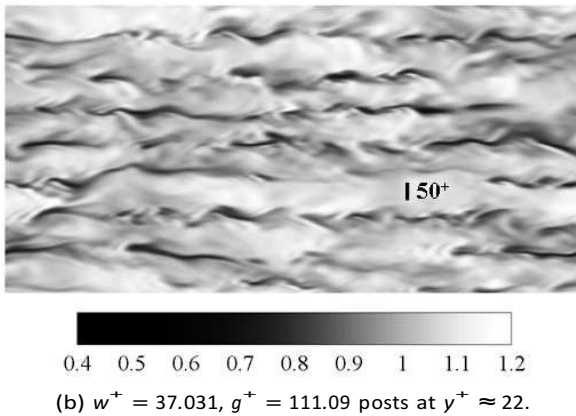
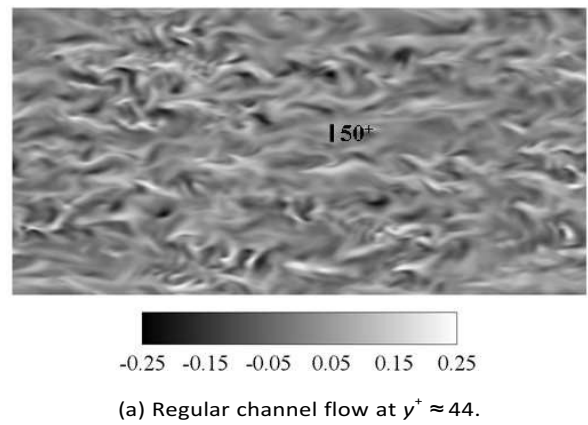
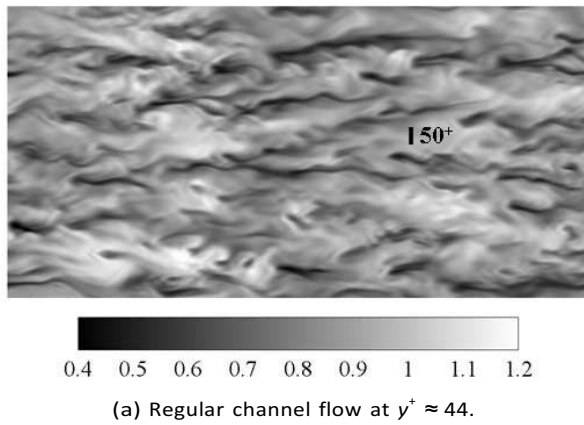


FIG. 36. $Re_\tau \approx 395$: Instantaneous streamwise velocity (U) contour slices (XZ), normalized by U_{bulk} , for a regular channel and one with $w^+ = 37.031$, $g^+ = 111.09$ posts. The slice in (a) is taken at $y^+ \approx 44$, while the slice in (b) is taken at $y^+ \approx 22$. Feature sizes and shapes are roughly equivalent.

FIG. 37. $Re_\tau \approx 395$: Instantaneous vertical (V) velocity contour slices (XZ), normalized by U_{bulk} , similar to those found in Figure 36, for the same geometries, taken at the same y^+ locations.

when compared with regular channel flow. The shear stress reduction (near 10%) found for $w/H = g/H = 0.1875$ ridges at $Re_\tau \approx 180$ closely matches the drag reduction reported in the experiments of Daniello *et al.*^{22,31}. The superhydrophobic surfaces alter the symmetry, peak magnitude, and peak locations of Reynolds stresses, largely in keeping with the redistribution of mean shear throughout the channel.

For all geometries investigated, and at all Reynolds numbers, the widely spaced posts outperformed the ridges by supporting a higher slip velocity and exhibiting a greater decrease in wall shear-stress. It appears as though the dimensionless slip velocity is independent of the Reynolds number (for fixed g^+ and w^+). Many of the results appear to have Reynolds number dependence when w/H and g/H are held fixed. The indications are, however, that when scaled appropriately (on g^+ and w^+) the flow behavior may be independent of Reynolds number.

Turbulent structures in the channel are shifted but otherwise largely unaffected by the superhydrophobic sur-

face. Examination of scaled R_{12} profiles, and of instantaneous streamwise and vertical velocity fields indicates that the turbulent structures remain intact, and are simply shifted toward the superhydrophobic surface. This is useful, as it means the existing theory and understanding of turbulent structures still applies to turbulent channel flow over superhydrophobic surfaces, and simply requires the turbulent structure locations to be modified. An understanding of this shift will allow engineers to model and predict the performance of superhydrophobic surfaces.

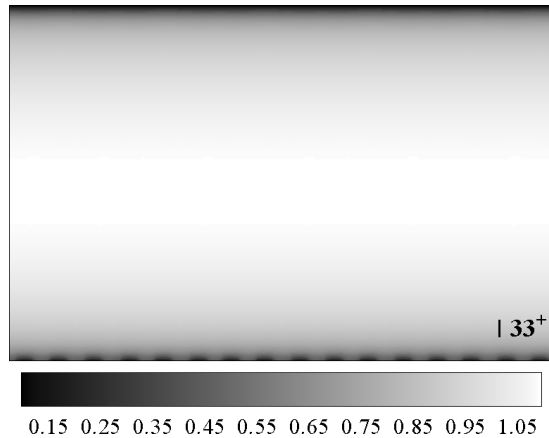


FIG. 38. $Re_\tau \approx 180$: Time-averaged streamwise (U) velocity contour slice (YZ , looking downstream), normalized by U_{bulk} , for $w^+ = g^+ = 33.75$ streamwise ridges. Note that the presence of the ridges alters the mean flow up until $y^+ \approx 10 - 15$.

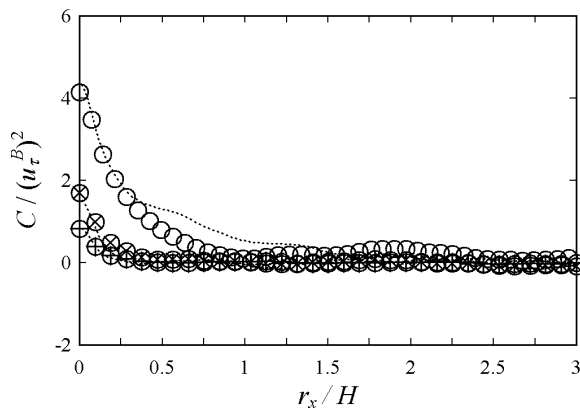
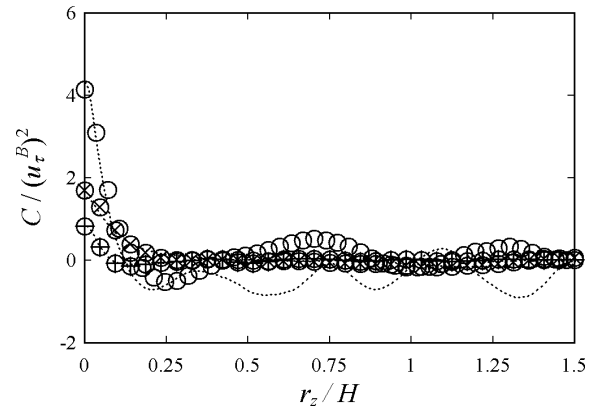


FIG. 39. $Re_\tau \approx 395$: A comparison of velocity correlation profiles in the streamwise (X) direction at $y^+ \approx 44$ obtained from a regular channel (\circ) and $w^+ = 37.031$, $g^+ = 111.09$ posts at $y^+ \approx 22$ (\times). Note that these are the same y^+ locations shown in Figures 36 and 37.

REFERENCES

- [1] Fu, Matt K., et al. "Liquid-infused surfaces as a passive method of turbulent drag reduction." *Journal of Fluid Mechanics* 824 (2017): 688-700.
- [2] Tang, Zuge, Behrad Zeinali, and Sarkew S. Abdulkareem. "Phase controlling of electromagnetically induced grating." *Laser Physics Letters* 19.5 (2022): 055204.
- [3] Golovin, Kevin B., et al. "Bioinspired surfaces for turbulent drag reduction." *Philosophical Transactions of the Royal Society A: Mathematical, Physical and Engineering Sciences* 374.2073 (2016): 20160189.
- [4] Arenas, Isnardo, et al. "Comparison between superhydrophobic, liquid infused and rough surfaces: a direct numerical simulation study." *Journal of Fluid Mechanics* 869 (2019): 500-525.
- [5] Lee, Jin, Thomas O. Jelly, and Tamer A. Zaki. "Effect of Reynolds number on turbulent drag reduction by superhydrophobic surface textures." *Flow, Turbulence and Combustion* 95 (2015): 277-300.
- [6] Zare, Saman, Behrad Zeinali Tajani, and Sheila Edalatpour.



- [7] Gómez-de-Segura, Garazi, and Ricardo García-Mayoral. "Effect of nonlocal electrical conductivity on near-field radiative heat transfer between graphene sheets." *Physical Review B* 105.12 (2022): 125416.
- [8] Park, Hyunwook, Hyungmin Park, and John Kim. "A numerical study of the effects of superhydrophobic surface on skin-friction drag in turbulent channel flow." *Physics of Fluids* 25.11 (2013): 110815.
- [9] Afroozeh, Abdolkarim, and Behrad Zeinali. "Improving the sensitivity of new passive optical fiber ring sensor based on meta-dielectric materials." *Optical Fiber Technology* 68 (2022): 102797.
- [10] Benschop, H. O. G., and W-P. Breugem. "Drag reduction by herringbone riblet texture in direct numerical simulations of turbulent channel flow." *Journal of Turbulence* 18.8 (2017): 717-759.
- [11] Fuaad, P. A., and K. Arul Prakash. "Enhanced drag-reduction over superhydrophobic surfaces with sinusoidal textures: A DNS study." *Computers & Fluids* 181 (2019): 208-223.
- [12] Zeinali, Behrad, and Jafar Ghazanfarian. "Turbulent flow over partially superhydrophobic underwater structures: The case of flow over sphere and step." *Ocean Engineering* 195 (2020): 106688.
- [13] Gose, James W., et al. "Characterization of superhydrophobic surfaces for drag reduction in turbulent flow." *Journal of Fluid Mechanics* 845 (2018): 560-580.
- [14] Alinovi, Edoardo, and Alessandro Bottaro. "Apparent slip and drag reduction for the flow over superhydrophobic and lubricant-impregnated surfaces." *Physical Review Fluids* 3.12 (2018): 124002.
- [15] Zeinali, Behrad, Jafar Ghazanfarian, and Bamdad Lessani. "Janus surface concept for three-dimensional turbulent flows." *Computers & Fluids* 170 (2018): 213-221.
- [16] Kumar, Susheel, Krishna Murari Pandey, and Kaushal Kumar Sharma. "Advances in drag-reduction methods related with boundary layer control—a review." *Materials Today: Proceedings* 45 (2021): 6694-6701.
- [17] Rad, Seyed Vahid, et al. "Drag reduction in internal turbulent flow by fabricating superhydrophobic Al₂O₃/waterborne polyurethane coatings." *Surface and Coatings Technology* 421 (2021): 127406.
- [18] Amini, Mahyar, and Zavareh Bozorgasl. "A Game Theory Method to Cyber-Threat Information Sharing in Cloud Computing Technology." *International Journal of Computer Science and Engineering Research* 11.4 (2023): 549-560.
- [19] Nazari Enjedani, Somayeh, and Mahyar Amini. "The role of

- traffic impact effect on transportation planning and sustainable traffic management in metropolitan regions ." *International Journal of Smart City Planning Research* 12.9 (2023): 688-700
- [20] Jahanbakhsh Javidi, Negar, and Mahyar Amini. "Evaluating the effect of supply chain management practice on implementation of halal agroindustry and competitive advantage for small and medium enterprises ." *International Journal of Computer Science and Information Technology* 15.6 (2023): 8997-9008
- [21] Amini, Mahyar, and Negar Jahanbakhsh Javidi. "A Multi-Perspective Framework Established on Diffusion of Innovation (DOI) Theory and Technology, Organization and Environment (TOE) Framework Toward Supply Chain Management System Based on Cloud Computing Technology for Small and Medium Enterprises ." *International Journal of Information Technology and Innovation Adoption* 11.8 (2023): 1217-1234
- [22] Amini, Mahyar and Ali Rahmani. "Agricultural databases evaluation with machine learning procedure." *Australian Journal of Engineering and Applied Science* 8.6 (2023): 39-50
- [23] Amini, Mahyar, and Ali Rahmani. "Machine learning process evaluating damage classification of composites." *International Journal of Science and Advanced Technology* 9.12 (2023): 240-250
- [24] Amini, Mahyar, Koosha Sharifani, and Ali Rahmani. "Machine Learning Model Towards Evaluating Data gathering methods in Manufacturing and Mechanical Engineering." *International Journal of Applied Science and Engineering Research* 15.4 (2023): 349-362.
- [25] Sharifani, Koosha and Amini, Mahyar and Akbari, Yaser and Aghajanzadeh Godarzi, Javad. "Operating Machine Learning across Natural Language Processing Techniques for Improvement of Fabricated News Model." *International Journal of Science and Information System Research* 12.9 (2022): 20-44.
- [26] Amini, Mahyar, et al. "MAHAMGOSTAR.COM AS A CASE STUDY FOR ADOPTION OF LARAVEL FRAMEWORK AS THE BEST PROGRAMMING TOOLS FOR PHP BASED WEB DEVELOPMENT FOR SMALL AND MEDIUM ENTERPRISES." *Journal of Innovation & Knowledge, ISSN* (2021): 100-110.
- [27] Zhang, Lixuan, et al. "Blockchain and cryptocurrency for announcing securely timestamped script submission and peer review reaction using the supply chain management ." *International Journal of Science and Information System* 9.3 (2021): 86-92.
- [28] Amini, Mahyar, and Aryati Bakri. "Cloud computing adoption by SMEs in the Malaysia: A multi-perspective framework based on DOI theory and TOE framework." *Journal of Information Technology & Information Systems Research (JITISR)* 9.2 (2015): 121-135.
- [29] Amini, Mahyar, and Nazli Sadat Safavi. "A Dynamic SLA Aware Heuristic Solution For IaaS Cloud Placement Problem Without Migration." *International Journal of Computer Science and Information Technologies* 6.11 (2014): 25-30.
- [30] Amini, Mahyar. "The factors that influence on adoption of cloud computing for small and medium enterprises." (2014).
- [31] Amini, Mahyar, et al. "Development of an instrument for assessing the impact of environmental context on adoption of cloud computing for small and medium enterprises." *Australian Journal of Basic and Applied Sciences (AJBAS)* 8.10 (2014): 129-135.
- [32] Amini, Mahyar, et al. "The role of top manager behaviours on adoption of cloud computing for small and medium enterprises." *Australian Journal of Basic and Applied Sciences (AJBAS)* 8.1 (2014): 490-498.
- [33] Amini, Mahyar, and Nazli Sadat Safavi. "A Dynamic SLA Aware Solution For IaaS Cloud Placement Problem Using Simulated Annealing." *International Journal of Computer Science and Information Technologies* 6.11 (2014): 52-57.
- [34] Sadat Safavi, Nazli, Nor Hidayati Zakaria, and Mahyar Amini. "The risk analysis of system selection and business process re-engineering towards the success of enterprise resource planning project for small and medium enterprise." *World Applied Sciences Journal (WASJ)* 31.9 (2014): 1669-1676.
- [35] Sadat Safavi, Nazli, Mahyar Amini, and Seyyed AmirAli Javadinia. "The determinant of adoption of enterprise resource planning for small and medium enterprises in Iran." *International Journal of Advanced Research in IT and Engineering (IJARIE)* 3.1 (2014): 1-8.
- [36] Sadat Safavi, Nazli, et al. "An effective model for evaluating organizational risk and cost in ERP implementation by SME." *IOSR Journal of Business and Management (IOSR-JBM)* 10.6 (2013): 70-75.
- [37] Safavi, Nazli Sadat, et al. "An effective model for evaluating organizational risk and cost in ERP implementation by SME." *IOSR Journal of Business and Management (IOSR-JBM)* 10.6 (2013): 61-66.
- [38] Amini, Mahyar, and Nazli Sadat Safavi. "Critical success factors for ERP implementation." *International Journal of Information Technology & Information Systems* 5.15 (2013): 1-23.
- [39] Amini, Mahyar, et al. "Agricultural development in IRAN base on cloud computing theory." *International Journal of Engineering Research & Technology (IJERT)* 2.6 (2013): 796-801.
- [40] Amini, Mahyar, et al. "Types of cloud computing (public and private) that transform the organization more effectively." *International Journal of Engineering Research & Technology (IJERT)* 2.5 (2013): 1263-1269.
- [41] Amini, Mahyar, and Nazli Sadat Safavi. "Cloud Computing Transform the Way of IT Delivers Services to the Organizations." *International Journal of Innovation & Management Science Research* 1.61 (2013): 1-5.
- [42] Abdollahzadegan, A., Che Hussin, A. R., Moshfegh Gohary, M., & Amini, M. (2013). The organizational critical success factors for adopting cloud computing in SMEs. *Journal of Information Systems Research and Innovation (JISRI)*, 4(1), 67-74.
- [43] Khoshraftar, Alireza, et al. "Improving The CRM System In Healthcare Organization." *International Journal of Computer Engineering & Sciences (IJCES)* 1.2 (2011): 28-35.
- [44] Li, Chang, et al. "Investigative success factors concerning adoption of blockchain technology on behalf of e-government improvement ." *International Journal of Basis Applied Science and Study* 11.6 (2021): 642-647.
- [45] Chen, Lee, et al. "Adoption of blockchain technology improving supply chain management system in small and medium cyber security enterprises ." *International Journal of Computer Science and Information Technology* 13.9 (2021): 2864-2870.